Journal of Alloys and Compounds 509 (2011) 5055–5060

Contents lists available at ScienceDirect

Journal of Alloys and Compounds

journal homepage: www.elsevier.com/locate/jallcom

Chemical synthesis, structural and magnetic properties of nano-structured Co–Zn–Fe–Cr ferrite

S.T. Alone [a], Sagar E. Shirsath [a,*], R.H. Kadam [b], K.M. Jadhav [a]

[a] Department of Physics, Dr. Babasaheb Ambedkar Marathwada University, Begampura, Aurangabad 431004 (MS), India
[b] Materials Research Laboratory, ShriKrishana Mahavidyalaya, Gunjoti, Osmanabad (MS), India

ARTICLE INFO

Article history:
Received 2 December 2010
Received in revised form 27 January 2011
Accepted 2 February 2011
Available online 1 March 2011

PACS:
75.50.Bb
61.05.cp
73.63.Bd

Keywords:
Nanostructured materials
Chemical synthesis
Magnetization
Transmission electron microscopy, TEM
Magnetic measurements

ABSTRACT

Nanoparticles of $Co_{1-x}Zn_xFe_{2-x}Cr_xO_4$ ($x = 0.0–0.5$) ferrites were prepared by chemical co-precipitation technique using metal sulphates. The structural and magnetic properties were investigated by means of X-ray diffraction (XRD), transmission electron microscopy (TEM), scanning electron microscopy (SEM), vibrating sample magnetometer (VSM), and AC susceptibility measurements. X-ray diffraction patterns indicate that the samples possess single phase cubic spinel structure. The lattice constant initially increases for $x \leq 0.3$ and thereafter for $x > 0.3$ it decreases with increasing x. The saturation magnetization (Ms), magneton number (n_B) and coercivity (Hc) decreases with increasing Cr–Zn content x. Curie temperature deduced from AC susceptibility data decreases with increasing x.

1. Introduction

Ferrites are technologically very important material having potential applications and interesting physics. They have been extensively investigated and being the subject of great interest because of their importance in many technological applications [1–3]. The important structural, electrical and magnetic properties of ferrite are responsible for their applications in various fields [4]. Over the past decade, magnetic nanoparticles have attracted much attention due to their properties from both application and theoretical points of view. The nanoparticles have many special magnetic and electrical properties that are significantly different from bulk particles [5]. The physical properties of the nanomaterials are predominantly controlled by the grain boundaries than by the grains [6]. The nanoparticles of ferrite can be prepared by various techniques such as citrate–nitrate combustion method [7], sol–gel route [8], pulsed laser ablation [9], and solvothermal process [10]. Ferrites, by virtue of their structure can accommodate a variety of cations at different sites enabling of wide variation in the electrical and magnetic properties. The interesting physical and chemical properties arise from their ability to distribute the cations among the tetrahedral (A) and octahedral [B] sites. Among the several spinel ferrites, cobalt ferrite ($CoFe_2O_4$) containing anisotropy ion is the most important ferrite to be used in several applications. It possesses the inverse spinel structure and its degree of inversion depends upon the heat treatment [11]. Many workers have studied the structural, electrical and magnetic properties of cobalt and cobalt-substituted ferrite [12,13]. It has been reported that the substitution of tetravalent ions in cobalt ferrite influences the structural, electrical and magnetic properties [14,15]. $ZnFe_2O_4$ is normal spinel while $CoFe_2O_4$ is an inverse spinel ferrite. Cobalt chromate is a normal spinel and Cr^{3+} has strong preference to octahedral B-site [16]. The substitution of trivalent ions like Cr^{3+} is likely to increase the resistivity and decrease the saturation magnetization [17]. It is also reported that the saturation magnetization (Ms), remanent magnetization (Mr), and coercive force (Hc) decreases monotonously whereas markedly improved the complex permeability and loss tangent when an appropriate amount of Cr^{3+} is substituted for Fe^{3+} ions [18]. The co-substitutional effect of magnetic Cr^{3+} and non-magnetic Al^{3+} at Fe site in cobalt ferrite is reported in the literature [19]. The method of preparation and heat treatment influences the electrical and magnetic properties. In the literature, studies on magnetic properties of $Co_{1-x}Al_xFe_{2-x}Cr_xO_4$ [20,21] and $CoCr_xFe_{2-2x}O_4$ [22] prepared by ceramic method have

* Corresponding author. Tel.: +91 2402240950; fax: +91 2402361270.
E-mail address: shirsathsagar@hotmail.com (S.E. Shirsath).

0925-8388/$ – see front matter © 2011 Elsevier B.V. All rights reserved.
doi:10.1016/j.jallcom.2011.02.006

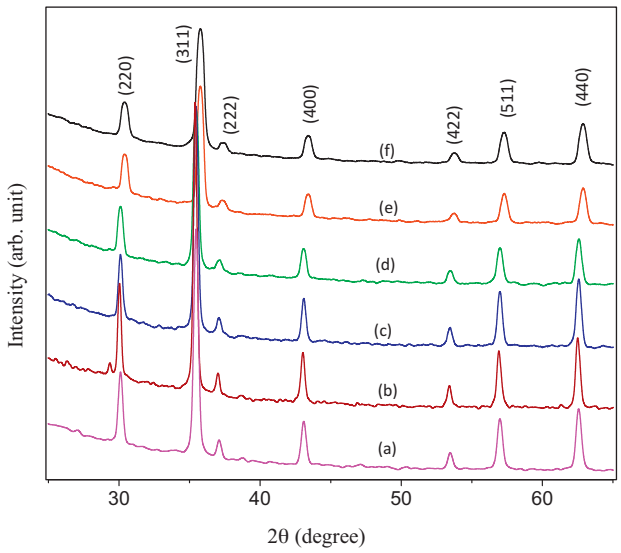

Fig. 1. XRD patterns of $x = 0.0–0.5$ of $Co_{1-x}Zn_xFe_{2-x}Cr_xO_4$.

been reported. To our knowledge, no reports are available in the literature for co-substitutional effect of magnetic Cr and non-magnetic Zn at octahedral and tetrahedral site respectively in cobalt ferrite. The literature survey revealed that the substitution of non magnetic ions in the spinel ferrite causes canting effect [23–25]. The ionic radius of Co^{2+} (0.74 Å) and Zn^{2+} (0.83 Å) are comparable and therefore Co^{2+} ions can easily replaced by Zn^{2+} ions. Cr^{3+} ions are magnetic having the magnetic moment of 3 μ_B. The ionic radius of Cr^{3+} is (0.63 Å) comparable with Fe^{3+} (0.67 Å). In the present paper, we report our results on structural and magnetic properties of non magnetic Zn^{2+} and magnetic Cr^{3+} substituted $CoFe_2O_4$ prepared by wet chemical co-precipitation method.

2. Experimental details

The spinel ferrite system with a chemical formula $Co_{1-x}Zn_xFe_{2-x}Cr_xO_4$ with variable composition ($x = 0.0–0.5$) is prepared by wet chemical co-precipitation method. The starting solutions were prepared by mixing of 50 ml of aqueous solution of $FeSO_4{\cdot}7H_2O$, $CoSO_4{\cdot}7H_2O$, $ZnSO_4{\cdot}7H_2O$ and $Cr_2(SO_4)_3{\cdot}6H_2O$ in stoichiometric proportion. A 2 M solution of NaOH was prepared as a precipitant. It has been suggested that the solubility product constant (K_{sp}) of all the constituents always exceed when the starting solution is added into the precipitant. Therefore, in order to achieve the simultaneous precipitation of all the hydroxide, the starting solution (pH ≈ 3) was added in to the solution of NaOH. Suspension (pH = 11) containing dark intermediate precipitation was formed. Then the suspension was heated and kept at 60 °C temperature, while oxygen gas was bubbled uniformly into the suspension to stir it and to promote the oxidation reaction until all the intermediate precipitant changed into the dark brownish precipitate of the spinel ferrite. The samples were filtered and washed several times by distilled water. The samples were annealed at 600 °C for 12 h for removing water and hydroxyl ions.

The X-ray powder diffraction patterns were recorded by using Cu Kα radiation on Philips X-ray difractometer (Model PW 3710) at room temperature. Particle size of the sintered powder samples was calculated using transmission electron microscope (TEM) (Model CM 200, Philips make). The microstructure and morphology of the ferrite powder were characterized by scanning electron microscopy (SEM) (Model JEOL-JSM 840). The magnetic data for these samples were obtained with the help of high field hysteresis loop technique [26]. The low field AC susceptibility measurements on powder samples were carried out in the temperature range 300–800 K using double coil setup [27] operating at a frequency of 263 Hz.

3. Results and discussion

3.1. Structural properties

The formation of single-phase cubic spinel structure was confirmed by X-ray diffraction patterns (XRD). All the peaks of the XRD pattern were indexed using Bragg's law. The XRD patterns of all the samples are shown in Fig. 1. XRD data was used to determine

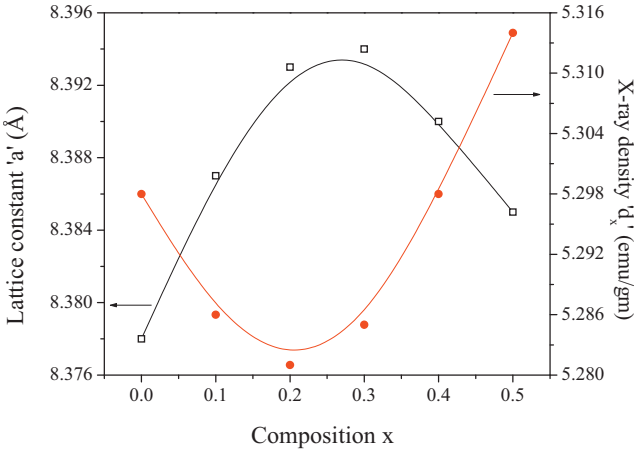

Fig. 2. Variation of lattice constant and X-ray density with composition.

structural parameters of all the samples. The lattice constant 'a' was determined using the following relation

$$a = d\sqrt{h^2 + k^2 + l^2} \quad (1)$$

where ($h\,k\,l$) are the Miller indices, d is the inter-planar spacing. The variation of lattice constant with composition x is shown in Fig. 2. It is clear from Fig. 2 that the lattice constant increases with increasing x up to $x = 0.3$. For $x > 0.3$ lattice constant decreases. Generally, in a solid solution series linear increase or decrease of lattice constant within the miscibility range with composition is observed [28]. This may results into initial rise in lattice constant up to $x = 0.3$ beyond which it decreases. This nonlinear behavior of lattice constant suggests that the ferrite system is not completely normal or inverse. In the present series, $Co_{1-x}Zn_xFe_{2-x}Cr_xO_4$, larger Fe^{3+} (0.67 Å) ions are replaced by smaller Cr^{3+} (0.63 Å) and smaller Co^{2+} ions are replaced by larger Zn^{2+} ions. However the replacement of Co^{2+} ions by Zn^{2+} ions is dominant up to $x = 0.3$. Hence we observed increase in lattice parameter beyond $x = 0.3$ replacements of Cr^{3+} ions are dominant. Hence we observed decrease in lattice parameter for $x > 0.3$. This may be due to cross substitution of ions. The X-ray density (d_x) was calculated according to the following relation

$$d_x = \frac{8M}{Na^3} \quad (2)$$

where M is molecular weight, N is Avogadro's number, and a is lattice constant. The variation of X-ray density with the composition x is shown in Fig. 2. The variation of X-ray density with x exhibits exactly reverse behavior as compared to the variation of lattice constant with x. This is because; X-ray density is inversely proportional to the lattice constant 'a^3'. The average particle size was calculated using the Scherrer equation [29]

$$t = \frac{0.9\lambda}{\beta\,\cos\theta} \quad (3)$$

where t particle size, λ is wavelength of the X-ray radiation, θ is Bragg's angle, and β is measure of broadening of diffraction due to size effect. The average particle sizes calculated using Eq. (3) are listed in Table 1, and it is observed that the particle size is decreases from 30 nm to 17 nm as Cr–Zn content increases. The bulk density (d_B) of the specimens has been determined by the hydro-static method. The values of the bulk density are shown in Fig. 3. This is evidence of decrease in particle size with increase in Cr–Zn content which led to increase in porosity. The percentage porosity 'P' of the sample was calculated using the values of X-ray density and bulk density, and using the relation, porosity (P) = $(d_x - d_B)/d_x$ [30]. Fig. 3 gives the variation of porosity as a function of Cr–Zn content x. It is clear from Fig. 3 that density of the samples decreases

Table 1
Particle size (t), the bond length of tetrahedral (A) site 'd_{AX}' and octahedral [B] site 'd_{BX}', tetrahedral edge 'd_{AXE}', shared octahedral edge 'd_{BXE}' and unshared octahedral edge 'd_{BXEU}'.

Comp. x	t (nm)		d_{AX}	d_{BX}	d_{AXE}	d_{BXE}	d_{BXEU}
	XRD	TEM					
0.0	30	26	1.901	2.048	3.104	2.819	2.970
0.1	27	23	1.903	2.050	3.107	2.822	2.973
0.2	24	21	1.904	2.051	3.109	2.825	2.975
0.3	22	18	1.905	2.052	3.110	2.825	2.975
0.4	20	16	1.904	2.051	3.108	2.824	2.974
0.5	17	15	1.902	2.049	3.106	2.822	2.972

and the porosity increases with increase in Cr–Zn composition x. The bond length of tetrahedral (A) site 'd_{AX}' and octahedral [B] site 'd_{BX}', tetrahedral edge 'd_{AXE}', shared octahedral edge 'd_{BXE}' and unshared octahedral edge 'd_{BXEU}' can be calculated by putting the experimental values of lattice parameter 'a' and oxygen positional parameter 'u' of each sample in the equations discussed elsewhere [31]. The values of d_{AX}, d_{BX}, d_{AXE}, d_{BXE} and d_{BXEU} are listed in Table 1 which indicates that the d_{AX} and d_{AXE} increases up $x = 0.3$ and then decreased after $x > 0.3$ with Cr–Zn content 'x', this may be due to Zn^{2+} replaces Co^{2+} of tetrahedral A site. Octahedral bond length 'd_{BX}', unshared octahedral edge 'd_{BXEU}' and shared octahedral edge 'd_{BXE}' increases up $x = 0.3$ and then decreased after $x > 0.3$ with Cr–Zn content 'x'. This could be related to the smaller radius of Cr^{3+} ions as compared to Fe^{3+} ions and the fact that Cr^{3+} occupies strongly tetrahedral B-site.

Fig. 4 shows TEM image of typical sample ($x = 0.3$), this image was used to study the particle size. The value of particle size is given in Table 1. The particle size is decreases from 26 nm to 15 nm with increasing Cr–Zn content x. As seen from Table 1, the particle size measured from XRD and TEM are in good agreement with each other. It can be considered that Zn^{2+} and Cr^{3+} ions may diffuse to the grain boundaries during the sintering process and inhibit grain growth by limiting grain mobility. Similar results were obtained for Cr substituted $Co_{0.5}Zn_{0.5}Fe_2O_4$ [32] and Zn^{2+}-doped TiO_2 nanoparticles [33]. Scanning electron micrographs (SEM) of the surfaces of the three compositions ($x = 0.1$, 0.3 and 0.5) are shown in Fig. 5. Each composition is characterized by a typical porous structure and small rounded grains. It is evident that the structure is affected by the Cr–Zn substitutions. It can be observed that the decrease in the grain size and an increase in porosity with increasing Cr and Zn substitutions. The Cr and Zn substituted ferrite exhibits the finest and uniform granulation (Fig. 5). The observed changes in grain size suggest that the incorporation of Cr–Zn in solid solution occurs during precipitation preparation which enables a better homogeneity

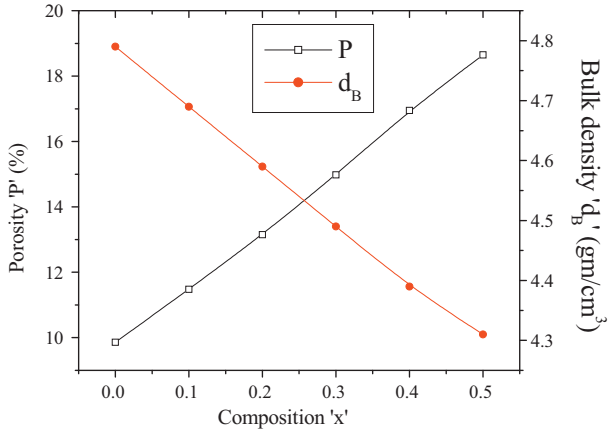

Fig. 3. Variation of porosity and bulk density.

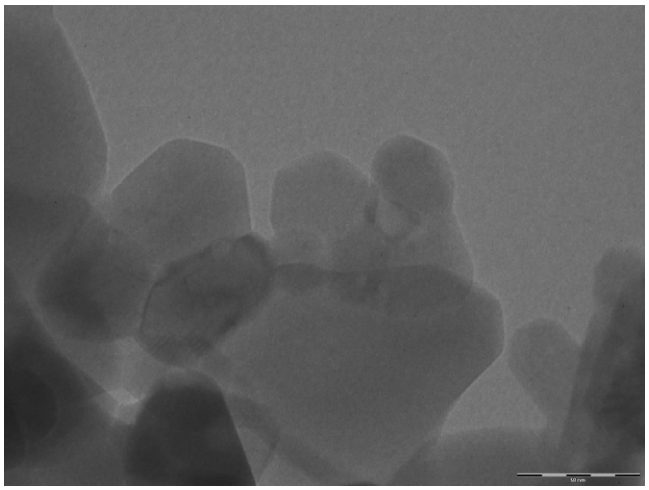

Fig. 4. TEM image of the typical samples $x = 0.2$.

in the powders and, hence, a more controlled microstructure is obtained. It can be observed from the SEM images that the prepared samples are amorphous and porous in nature. The particles were well distributed and slightly agglomerated. The agglomeration is the indication of high reactivity of the prepared sample with the heat treatment and it may also be come from the magnetostatic interaction between particles [34–37]. The Cr and Zn incorporation lead to radical changes in microstructure (Fig. 5) which consist in the followings:

(i) A significant decrease in the particle size, from 26 nm to about 15 nm;
(ii) The formation of grain bridges around the large pores and interconnected pores in the form of capillary tubes between the grain chains;
(iii) It is possible that the presence of the foreign phase inhibits the grain growth and agglomeration process.

3.2. Magnetic properties

The substitution of Zn and Cr ions, which is having a preferential A- and B-site occupancy respectively, results in the reduction of the exchange interaction between A- and B-sites. Hence, by varying the degree of Zn and Cr substitution the magnetic properties of the fine particles can be varied. Fig. 6 shows the room temperature (300 K) hysteresis loop for the typical samples ($x = 0.0$, 0.3 and 0.5). The values of saturation magnetization (Ms) coercivity (Hc) and magneton number (n_B) (saturation magnetization per formula unit 'μ_B') obtained from hysteresis loop technique are summarized in Table 2. The observed magneton number (n_B Obs.) was calculated

Table 2
Saturation magnetization (Ms), coercivity (Hc), observed and calculated magneton number (n_B), Yafet–Kittel angle (θ_{YK}) and Curie temperature (T_C) for $Co_{1-x}Zn_xFe_{2-x}Cr_xO_4$.

Comp. x	Ms (emu/g)	Hc (Oe)	n_B (μ_B)		θ_{YK} (0°)	T_C (K)
			Obs.	Cal.		
0.0	46.62	1453	1.959	3.00	–	776
0.1	59.57	1052	2.568	3.50	–	720
0.2	82.88	641	3.489	4.00	–	652
0.3	85.47	382	3.603	4.50	27.39	574
0.4	49.86	213	2.104	5.00	50.36	519
0.5	17.61	135	0.744	5.50	82.81	459

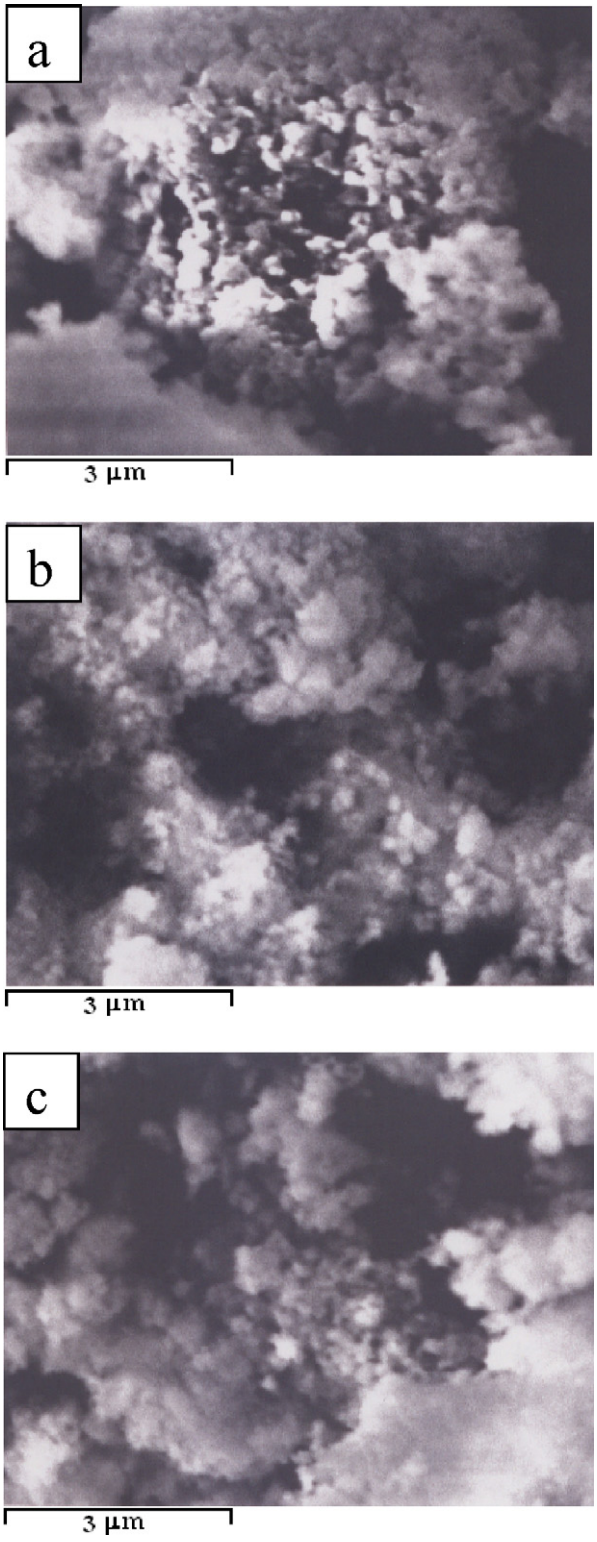

Fig. 5. SEM images of the typical samples (a) $x = 0.1$, (b) $x = 0.3$ and (c) $x = 0.5$.

using the formula:

$$n_B = \frac{\text{Molecular weight (Mw)} \times \text{saturation magnetization (Ms)}}{5585} \quad (4)$$

It is observed from Table 2 that saturation magnetization and observed magneton number increases up to $x = 0.3$ and then decreases as Zn^{2+} and Cr^{3+} ions increases. In the present system

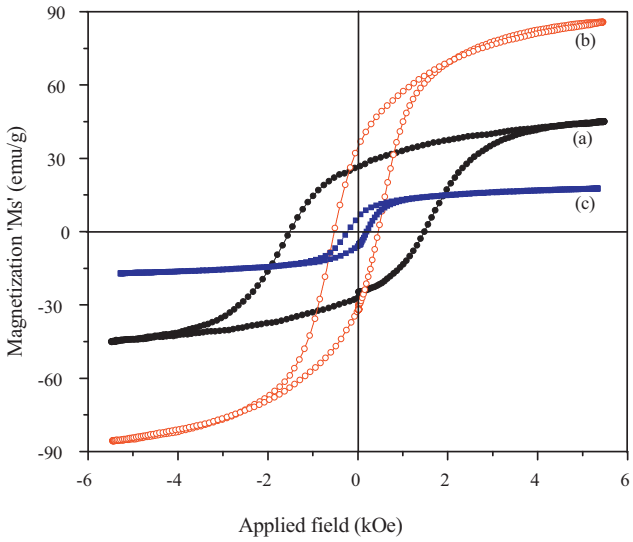

Fig. 6. Magnetization curve for (a) $x = 0.0$, (b) $x = 0.3$ and (c) $x = 0.5$.

zinc ions of magnetic moment (0 μ_B) occupies tetrahedral A-site and push the Fe^{3+} ions of magnetic moment (5 μ_B) to octahedral B-site. This migration of Fe^{3+} ions from A-site to B-site increases the net magnetic moment of B-site, resulting overall increase in saturation magnetization up to $x = 0.3$. The decreasing trend for $x > 0.3$ is due to the fact that after a certain amount of zinc concentration, there start fluctuations in the number of ratio of zinc and ferric ions on the tetrahedral sites surrounding the various octahedral sites i.e. fluctuations in the tetrahedral-octahedral interactions [10]. Also in the present case Co^{2+} (3 μ_B) are replaced by Zn^{2+} (0 μ_B) and Fe^{3+} (5 μ_B) are replaced by Cr^{3+} (3 μ_B) ions, i.e. magnetic ions are replaced by comparatively non magnetic ions. This results in the weakening of A–B interaction whereas B–B interaction changes from ferromagnetic to antiferromagnetic state. The variation of n_B with Zn–Cr content x can be understood by considering the cation distribution and the anti-parallel spin alignments, the two sub-lattice sites following from the Neel's molecular model of ferrimagnetisms. According to Neel's two sub-lattice model of ferrimagnetisms [38], Neel's calculated magnetic moment in μB, n_B^N is expressed as,

$$n_B^N = M_B - M_A \quad (5)$$

where M_B and M_A are the magnetic moments of B and A sub-lattice respectively. n_B^N values for $x = 0.0$–0.5 were calculated using above equation and also taking the ionic magnetic moment of Fe^{3+} (5 μ_B), Zn^{2+} (0 μ_B), Cr^{3+} (3 μ_B) and Co^{3+} (3 μ_B). The values of calculated magnetic moment n_B^N for $x = 0.0$–0.3 are in good agreement with the observed magnetic moment confirming the collinear spin ordering, while for $x = 0.3$–0.5 values of observed and calculated magnetic moment are different from each other. Fig. 7 indicates that significant canting exists on B site suggesting magnetic structure to be non-collinear. Thus, the change of spin ordering from collinear to non-collinear display a strong influence on the variation of magnetic moment per formula unit as observed by magnetization with Cr–Zn content. The initial increase in observed magnetic moment with Cr–Zn content x is explained on the basis of Neel's theory, but decrease in observed magnetic moment after $x > 0.3$ indicates a possibility of non-collinear spin structure in the system which can be explained on the basis of three sub-lattice model suggested by Yafet–Kittel [39]. Yafet–Kittel (Y–K) angles have been calculated using the following formula

$$n_B = M_B \cos\theta_{YK} - M_A \quad (6)$$

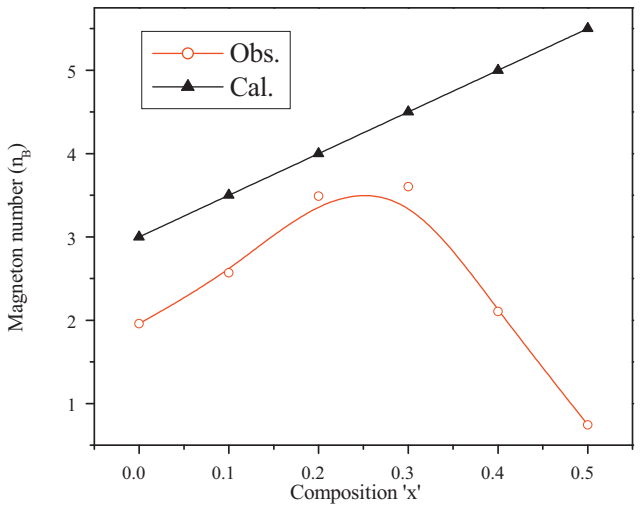

Fig. 7. Variation of observed and calculated magnetic moment of $Co_{1-x}Zn_xFe_{2-x}Cr_xO_4$.

The value of Y–K angles for samples with $x = 0.0–0.2$ is not observed (Table 2) which indicates that magnetization of this composition can be explained with Neel's two lattice theory. The increase in Y–K angles with further increase in Cr–Zn content suggest that magnetization in these ferrites can be explained on the basis of canted spin model. The increase of Y–K angles with Zn content indicates the fact that triangular spin arrangement is suitable on the B-site leading to the reduction in A–B interaction.

Coercivity in Co–Zn–Fe–Cr ferrites is given in Table 2. It decreases with the increase in Cr–Zn concentration. This is due to the fact that Hc decreases with the decrease in magnetocrystalline anisotropy. The magnetocrystalline anisotropy constant (K_1) is negative for both Cr and Zn ferrites. The absolute value of K_1 is larger for Co ferrites than that of Cr and Zn ferrites. The total anisotropy is equal to the sum of their individual anisotropies. So K_1 and hence coercivity decreases with the increase in Cr–Zn concentration.

The plots of AC susceptibility $\chi_{ac}(T)/\chi_{ac}(RT)$ against temperature T for the samples $x = 0.0–0.5$ are shown in Fig. 8. For $x \leq 0.3$ the plots of $\chi_{ac}(T)$ data display two peaks, one sharp peak near the Curie temperature (T_C) and another broad peak at much lower temperature. For $x \geq 0.4–0.5$ only a broad maximum is observed. Zubov et al. [40] have studied the temperature dependence of AC susceptibility for pure cobalt ferrite and they have observed two peaks one near Curie temperature ($T_C = 776$ K) and second peak at 533 K. This second peak is referred to as the isotropic peak [41], which could be seen clearly for a magnetic material in a multi-domain state only if the material has the temperature at which the magneto-crystalline anisotropy is zero [42]. Beyond the temperature at which the isotropic peak occurs, the shape anisotropy will be dominant and as a result the coercive force arises. The addition of Zn and Cr to pure $CoFe_2O_4$ reduces the coercive force, which results in decrease in the peak value of susceptibility. Further addition of Zn and Cr shows broad maxima near T_C and the suppression of the isotropic peak. Therefore, it can be concluded that the samples of these system contain multi-domain spin cluster. The value of Curie temperature is given in Table 2. The Curie temperature obtained from χ_T/χ_{RT} plots decreases with increasing Zn–Cr concentration x which suggest decrease in A–B interaction.

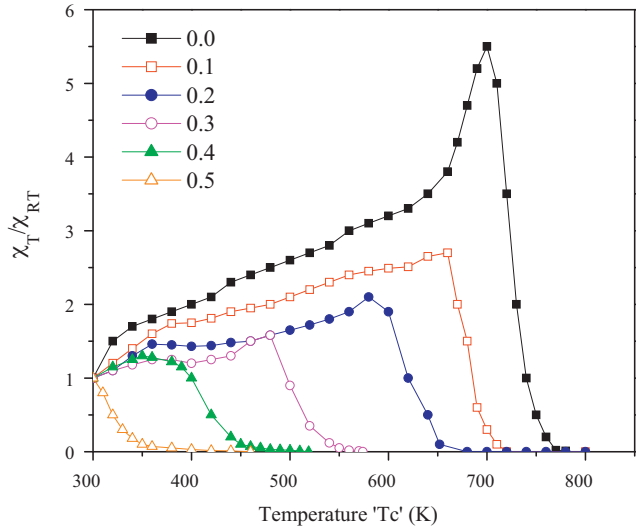

Fig. 8. Plots of χ_T/χ_{RT} versus temperature.

4. Conclusions

Analysis of XRD patterns confirms that all the samples possess single phase cubic spinel structure. The wet-chemical co-precipitation method yields fine particles of the order of few nanometers which are confirmed by TEM analysis. Lattice constant increases up to $x = 0.3$ and thereafter it decreases, this behavior suggests that the ferrite system is not completely normal or inverse. Magnetizations and observed magneton number increases up to $x \leq 0.3$ and then decreases with increasing Cr–Zn content. Neel's model is applicable up to $x = 0.3$, above which Yafet–Kittel model can be applied and it decreases with increasing Cr–Zn content. Thermal variation of AC susceptibility shows a normal ferrimagnetic behavior which reduces with increasing Cr–Zn content. Curie temperature determined from AC susceptibility plots decreases with increasing Cr–Zn content. The decrease in Curie temperature reflects the weakening in A–B interaction of the respective ions.

References

[1] A. Goldman, Modern Ferrite Technology, 2nd ed., Springer, New York, 2006.
[2] V.G. Patil, S.E. Shirsath, S.D. More, S.J. Shukla, K.M. Jadhav, J. Alloys Compd. 488 (2010) 199.
[3] P. Hu, H.B. Yang, D.A. Pan, H. Wang, J.J. Tian, S.G. Zhang, X.F. Wang, A.A. Volinsky, J. Magn. Magn. Mater. 322 (2010) 173.
[4] S.M. Patange, S.E. Shirsath, B.G. Toksha, S.S. Jadhav, S.J. Shukla, K.M. Jadhav, Appl. Phys. A 95 (2009) 429.
[5] S.M. Patange, S.E. Shirsath, B.G. Toksha, S.S. Jadhav, K.M. Jadhav, J. Appl. Phys. 106 (2009) 023914.
[6] K.M. Batoo, S. Kumar, C.G. Lee, Alimuddin, Curr. Appl. Phys. 9 (2009) 1397.
[7] R.C. Kambale, N.R. Adhate, B.K. Chougule, Y.D. Kolekar, J. Alloys Compd. 491 (2010) 372.
[8] P.P. Hankare, R.P. Patil, U.B. Sankpal, S.D. Jadhav, K.M. Garadkar, S.N. Achary, J. Alloys Compd. 509 (2011) 276.
[9] K. Praveena, K. Sadhana, S.R. Murthy, J. Alloys Compd. 492 (2010) 245.
[10] A. Chaudhuri, S. Mitra, M. Mandal, K. Mandal, J. Alloys Compd. 491 (2010) 703.
[11] G.A. Sawataky, F. Van Woude, A.H. Morrish, J. Appl. Phys. 39 (1968) 1204.
[12] J. Nogues, T. Phig, R.B. Jotania, R.V. Upadyay, R.G. Kulkarni, K.V. Rao, J. Magn. Magn. Mater. 99 (1991) 275.
[13] B.G. Toksha, S.E. Shirsath, S.M. Patange, K.M. Jadhav, Solid State Commun. 147 (2008) 479.
[14] J. Smit, H.P.J. Wijn, Ferrites, Philips Technical Library, Holland, 1959.
[15] V.A. Ioffe, G.I. Khvostenko, Z.N. Zoon, Sov. Phys. JTP 27 (1957) 1985.
[16] L. Zhao, W. Xu, H. Yang, L. Yu, Curr. Appl. Phys. 8 (2008) 36.
[17] F.N. Bradley, Materials for Magnetic Functions, Hayden, New York, 1971, p. 78.
[18] Fu Yen-Pei, Jpn. J. Appl. Phys. 46 (2007) 7314.
[19] S.A. Patil, V.C. Mahajan, A.K. Ghatge, S.D. Lotke, Matt. Chem. Phys. 57 (1998) 86.
[20] B.S. Trivedi, R.G. Kulkarni, Solid State Commun. 86 (1993) 327.
[21] K.M. Jadhav, V.B. Kawade, K.B. Modi, G.K. Bichile, R.G. Kulkarni, Physica B 291 (2000) 379.
[22] H. Mohan, I.A. Shaikh, R.G. Kulkarni, Physica B 217 (1996) 292.
[23] D.R. Shengule, K.M. Jadhav, G.K. Bichile, Ind. J. Phys. 78 (2004) 1221.
[24] M.A. Ahmed, K.A. Darwish, E.H. El-Khawas, Ind. J. Phys. 71A (1997) 19.
[25] S.K. Mohammad Yusuf, V.C. Sahni, L. Madhav Rao, J. Phys. Condens. Matter 7 (1995) 873.
[26] C. Radhakrishanmurthy, S.D. Likhite, N.P. Sastry, Philips Mag. 23 (1971) 503.
[27] C. Radhakrishanmurthy, S.D. Likhite, P.W. Sahastrabudhe, Ind. Acad. Sci. A 87 (1978) 245.

[28] C.G. Whinfrey, D.W. Eckort, A. Tayber, J. Am. Chem. Soc. 82 (1960) 2695.
[29] H.P. Klug, L.E. Alexander, X-Ray Diffraction Procedures for Polycrystalline and Amorphous Materials, Wiley, New York, NY, 1997, p. 637.
[30] S.E. Shirsath, B.G. Toksha, K.M. Jadhav, Mater. Chem. Phys. 117 (2009) 163.
[31] S.S. Jadhav, S.E. Shirsath, B.G. Toksha, S.M. Patange, S.J. Shukla, K.M. Jadhav, Int. J. Mod. Phys. 23 (2009) 5629.
[32] R.K. Sharma, O. Suwalka, N. Lakshmi, K. Venugopalan, A. Banerjee, P.A. Joy, Mater. Lett. 59 (2005) 3402.
[33] G. Liu, X. Zhang, Y. Xu, X. Niu, L. Zheng, X. Ding, Chemosphere 59 (2005) 1367.
[34] C.A. Ross, Annu. Rev. Mater. Res. 31 (2001) 203.
[35] S.A. Majetich, M. Sachan, J. Phys. D: Appl. Phys. 39 (2006) R407.
[36] K.G. Kornev, D. Halverson, G. Korneva, Y. Gogotsi, G. Friedman, Appl. Phys. Lett. 92 (2008) 233117.
[37] M. Beleggia, S. Tandon, Y. Zhu, M. De Graef, J. Magn. Magn. Mater. 278 (2004) 270.
[38] L. Neel, C.R. Acad. Sci. Paris 230 (1950) 375.
[39] Y. Yafet, C. Kittel, Phys. Rev. 90 (1952) 295.
[40] V.V. Zubov, M.L. Skrebneva, Fiz. Met. Metalloved. 22 (1966) 45.
[41] C. Radhakrishanmurthy, S.D. Likhite, Earth Planet. Sci. Lett. 7 (1970) 389.
[42] S.A. Plotinikov, G.M. Prikhodkine, Sov. Phys. Solid State 7 (1965) 241.